

# *The Effect of Texture Shape on the Load-Carrying Capacity of Gas-Lubricated Parallel Slider Bearings*

**Mingfeng Qiu, Adis Delic & Bart Raeymaekers**

**Tribology Letters**

ISSN 1023-8883

Volume 48

Number 3

Tribol Lett (2012) 48:315-327

DOI 10.1007/s11249-012-0027-4



**Your article is protected by copyright and all rights are held exclusively by Springer Science+Business Media, LLC. This e-offprint is for personal use only and shall not be self-archived in electronic repositories. If you wish to self-archive your work, please use the accepted author's version for posting to your own website or your institution's repository. You may further deposit the accepted author's version on a funder's repository at a funder's request, provided it is not made publicly available until 12 months after publication.**

# The Effect of Texture Shape on the Load-Carrying Capacity of Gas-Lubricated Parallel Slider Bearings

Mingfeng Qiu · Adis Delic · Bart Raeymaekers

Received: 25 May 2012 / Accepted: 4 August 2012 / Published online: 19 August 2012  
© Springer Science+Business Media, LLC 2012

**Abstract** Surface texturing is used to increase hydrodynamic pressure and reduce friction and wear between gas-lubricated parallel sliding surfaces. The shape, geometry, and density of the patterned microtexture features (“dimples”) play a key role in the tribological performance of the textured slider bearings. The objective of this paper is to compare the load-carrying capacity of commonly used dimple shapes for gas-lubricated textured parallel slider bearings. Six different texture shapes are considered, including spherical, ellipsoidal, circular, elliptical, triangular, and chevron-shaped dimples. The pressure distribution and load-carrying capacity generated by different texture shapes are simulated using the compressible Reynolds equation over a domain containing a column of ten dimples. The texture geometry and density are optimized in terms of maximum load-carrying capacity for each individual dimple shape, as a function of operating parameters such as relative velocity and spacing between the two sliding surfaces. The maximum load-carrying capacity of each individual texture shape—with optimized geometry and density—is then compared relative to each other. It is concluded that the ellipsoidal shape results in the highest load-carrying capacity, and the optimal geometry and density are found to be almost independent of the operating conditions.

**Keywords** Hydrodynamic lubrication · Gas bearings · Surface texturing

## List of Symbols

$a, b$	Half-length of the ellipse axes in the $x$ - and $y$ -direction
$c$	Minimum spacing between parallel surfaces
$K$	Chevron shape ratio (ratio of length of inner and outer equilateral triangle forming the chevron shape) $0 \leq K \leq 1$
$H(X, Y)$	Non-dimensional local spacing $H = h/c$
$h(x, y)$	Local spacing
$h_p$	Dimple depth
$N$	Number of dimples in a column
$n$	Number of intervals in one direction on the square computational grid of a single dimple cell
$P(X, Y)$	Non-dimensional pressure, $P = p/p_a$
$p(x, y)$	Bearing pressure
$p_0$	Atmospheric pressure
$p_{\text{avg}}$	Average bearing pressure
$r_1$	Half-length of the square unit cell
$r_p$	Dimple characteristic radius
$S_p$	Texture density
$U$	Sliding velocity
$X, Y$	Non-dimensional Cartesian coordinates, $X = x/r_p, Y = y/r_p$
$x, y$	Cartesian coordinates
$\Delta x$	Computational grid interval length
$\delta$	Non-dimensional minimum spacing between parallel surfaces, $\delta = c/2r_p$
$\varepsilon$	Dimple aspect ratio for spherical, circular, triangular, and chevron-shaped dimples, $\varepsilon = h_p/2r_p$
$\varepsilon_1, \varepsilon_2$	Dimple aspect ratios for ellipsoidal and elliptical dimples, $\varepsilon_1 = h_p/2a, \varepsilon_2 = h_p/2b$
$\theta$	Angle of inclination of the dimple wall due to numerical discretization
$\lambda$	Flow parameter, $\lambda = 3\mu U/2r_p$

M. Qiu · A. Delic · B. Raeymaekers (✉)  
Department of Mechanical Engineering, University of Utah,  
Salt Lake City, UT 84112, USA  
e-mail: bart.raeymaekers@utah.edu

$\mu$	Gas dynamic viscosity
$\rho$	Gas density

## 1 Introduction

Lubrication between two parallel sliding surfaces separated by a micro- or nanoscale gap is of critical importance for precision machinery and design of intricate and complex micro- and nanoscale sliding interfaces. Surface texturing has been widely recognized as an effective way to reduce friction and wear between sliding surfaces separated by a thin compressible or incompressible lubricant film. A patterned microtexture on one of the sliding surfaces, usually implemented as a dense array of microsized concave features (which are referred to as “dimples”), increases the pressure in the lubricant, thereby increasing the load-carrying capacity of the bearing and reducing friction. These microsized dimples create an array of microsized hydrodynamic bearings to generate pressure in the interface between two parallel sliding surfaces [1–3], and they form microscale wear particle traps to prevent wear particles from generating abrasive wear [4, 5]. Several published studies document that the transition between boundary and hydrodynamic lubrication occurs at a lower sliding velocity when using a textured surface as compared to a smooth surface [6–10]. Significant results reporting friction reduction and enhanced load-carrying capacity have been presented for incompressible fluid film bearings including journal bearings [11–13], thrust bearings [14–17], piston rings [18], and mechanical seals [2, 19–21]. Furthermore, surface texturing has been successfully applied to compressible fluid film bearings, such as in hydrostatic mechanical seals [22], and the interface between magnetic tape and a cylindrical guide in a magnetic tape drive [10, 23]. Different manufacturing techniques have been employed to create a patterned microtexture on engineering surfaces such as vibro-rolling [24] and fabrication of undulated surfaces [25]. More recently developed techniques include reactive ion etching (RIE) [26], abrasive jet machining [27], lithography and anisotropic etching [28], LIGA [29], and vibro-mechanical texturing [30]. Laser surface texturing (LST) [1, 31–36] seems to be the most commonly used technique.

It is oftentimes critical to optimize the geometry of the microtexture to maximize the load-carrying capacity of the bearing, minimize friction between the sliding surfaces (and thus minimize energy consumption), and extend the life of mechanical components by reducing wear. The optimal microtexture geometry for a specific set of operating conditions has been investigated in several studies,

analytically [17, 37], experimentally [2, 8, 9, 14, 26, 38, 39], and numerically [2, 18, 23, 40]. These studies revealed that for any particular dimple shape, the texture density defined as the surface area covered by dimples relative to the total area of the sliding interface, and the aspect ratio of the dimples defined as the ratio of the dimple depth over the diameter, play a critical role in determining the effectiveness of the patterned microtexture to increase the bearing pressure and reduce friction. Only a few of these studies tested different dimple shapes [9, 39]. Some authors have compared the tribological performance of different dimple shapes using numerical simulation, mainly for incompressible lubricant. Siripuram and Stephens studied concave dimples with seven different shapes and investigated the effect of texture density on the pressure in the bearing [41]. They concluded that the texture density rather than the shape plays an important role in terms of reducing the friction coefficient. In their study, however, the depth of different dimple shapes was kept constant, potentially preventing each shape from reaching its optimal geometry, since the optimum for different geometries and/or shapes may not necessarily be achieved at a constant dimple depth. Yu et al. [42] simulated different dimple shapes with a flat bottom profile including circular, elliptical, and triangular dimples. They found that the shape indeed makes a difference in terms of load-carrying capacity, and identified the elliptical shape placed with the long axis perpendicular to the flow direction to be optimal. However, their analysis assumed similar limitations as Siripuram et al.’s work such as a constrained texture density and dimple depth.

While the existing literature sheds light on the effect of surface microtexturing on increasing the bearing load-carrying capacity and reducing friction, a general, unconstrained comparison of the bearing load-carrying capacity as a function of the dimple shape is currently not available. Most of the published studies only considered one dimple shape (e.g., spherical, square, triangular) and focused on a specific application. Moreover, different studies used a variety of operating conditions, making a fair and direct comparison of dimple shapes and geometries very difficult. When comparing different microtexture shapes, existing studies typically constrained the optimization to constant dimple depth and/or texture density, thereby not necessarily comparing the optimized geometry for each different dimple shape with each other. Hence, the objective of this paper is to provide an unbiased comparison of commonly used dimple shapes for the general case of gas-lubricated, textured parallel slider bearings. The compressible Reynolds equation is solved numerically for six different dimple shapes, and the geometry of each different shape is optimized to maximize the load-carrying capacity of the textured parallel slider bearing, without limiting the geometric parameters and the texture density. The

performance of the individually optimized shapes is then compared relative to each other.

## 2 Analytical Model

### 2.1 Model Description and Boundary Conditions

Figure 1 shows a schematic of the model that is implemented. A column of dimples represents the patterned microtexture on one of the mating surfaces of the parallel slider bearing. The second surface is flat and moves relative to the textured surface with velocity  $U$ . Figure 1a shows a cross-section of the textured parallel slider bearing through the centerline of the column of dimples. The minimum spacing between the bearing surfaces is indicated as  $c$ , while the local spacing is denoted by  $h(x,y)$ , where  $x$  and  $y$  are Cartesian coordinates as indicated in the figure. Figure 1b shows a top view of a column of dimples. Each dimple is contained in a square unit cell of width  $2r_1$ . A dimple shape is characterized by its contour and bottom profile.

The following assumptions are made in the model: (1) each dimple has an identical shape (e.g., spherical) and is positioned in the center of the square unit cell (Fig. 1). (2) Air at room temperature is used as lubricant, and inertia effects are neglected because the relative velocity between the sliding surfaces  $U$  and the minimum bearing spacing  $c$  are kept small. For instance, an air lubricated magnetic tape moves at a speed on the order of 1 m/s over a guide in a tape drive, with tape/guide spacing of approximately  $10^{-6}$  m [43]. In this case, the Reynolds number  $\rho Uc/\mu$  is on the order of 0.1, which means that the inertia forces are one order of magnitude smaller than the viscous forces and can be neglected. On the other hand, the spacing  $c$  is approximately two orders of magnitude larger than the mean free path of air at room temperature, so gas

rarefaction effects and slip at the solid wall boundary are neglected. (3) While only one column of dimples is simulated, the texture pattern consists of many columns of dimples. A symmetric boundary condition is implemented to account for the presence of dimples adjacent to the single column that is simulated. (4) The minimum spacing  $c$  between the sliding surfaces is sufficient to avoid asperity contact and, thus, hydrodynamic lubrication is maintained.

Based on these assumptions, the classical steady-state two-dimensional compressible Reynolds equation is given as [44]

$$\frac{\partial}{\partial x} \left( \rho h^3 \frac{\partial p}{\partial x} \right) + \frac{\partial}{\partial y} \left( \rho h^3 \frac{\partial p}{\partial y} \right) = 6\mu U \frac{\partial(\rho h)}{\partial x}, \quad (1)$$

where  $x$  and  $y$  are Cartesian coordinates as indicated in Fig. 1,  $p(x,y)$  is the air-bearing pressure,  $h(x,y)$  is the local clearance,  $\mu$  is the dynamic viscosity of air, and  $U$  is the relative sliding velocity between the textured and the flat surfaces, respectively (in the  $x$ -direction). Equation (1) can be written in non-dimensional form as

$$\frac{\partial}{\partial X} \left( PH^3 \frac{\partial P}{\partial X} \right) + \frac{\partial}{\partial Y} \left( PH^3 \frac{\partial P}{\partial Y} \right) = \frac{\lambda}{\delta^2} \frac{\partial(PH)}{\partial X}, \quad (2)$$

where  $X = x/r_p$ ,  $Y = y/r_p$ ,  $P(X,Y) = p(x,y)/p_0$ ,  $H(X,Y) = h(x,y)/c$ , and  $p_0$  denotes the atmospheric pressure. The characteristic radius of the dimple  $r_p$  is defined for different texture shapes in Sect. 2.2 of this paper. In addition, the flow factor  $\lambda = 3\mu U/2r_p p_0$  and non-dimensional minimum spacing  $\delta = c/2r_p$ , define the operating conditions. At the inlet and outlet of the dimple column, the pressure is equal to the atmospheric pressure. On the other hand, the texture pattern is periodic in the direction perpendicular to the flow direction to account for the presence of dimples adjacent to the simulation domain. Hence, the pressure profile is symmetric with respect to the lateral edge of the unit cell. The boundary conditions are expressed as

$$P\left(-\frac{r_1}{r_p}, Y\right) = P\left(\left(N - \frac{1}{2}\right) \frac{2r_1}{r_p}, Y\right) = 1, \quad (3a)$$

$$\frac{\partial P}{\partial Y} \left( X, -\frac{r_1}{r_p} \right) = \frac{\partial P}{\partial Y} \left( X, \frac{r_1}{r_p} \right) = 0, \quad (3b)$$

with respect to the origin of the coordinate system depicted in Fig. 1.  $N$  is the number of dimple cells in one column of dimples, and  $r_1$  is half the length of a unit cell (Fig. 1). The pressure distribution in the gas bearing is found by numerically solving Eqs. (2) and (3) for given operating parameters  $\lambda$ ,  $\delta$ , and local clearance  $H(X,Y)$ , which depends on the dimple shape. The load-carrying capacity per unit area is represented by the non-dimensional net average pressure, or the so-called gauge pressure, i.e., the average bearing pressure calculated over a column of ten dimples minus the atmospheric pressure.

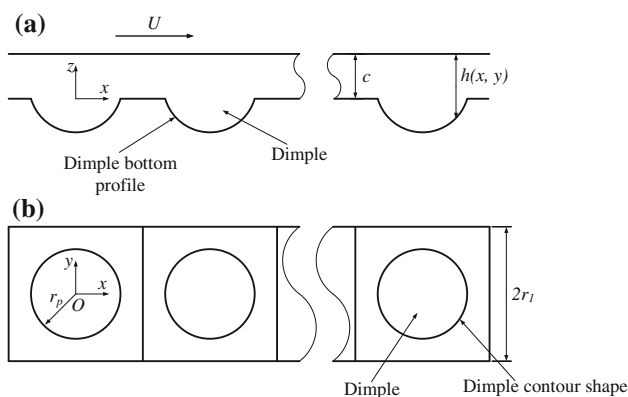


**Fig. 1** A column of spherical dimples: **a** cross-section through center line, **b** top view

### 2.2 Dimple Shape and Geometry

Six different dimple shapes are considered in this study: ellipsoid and sphere, ellipse and circle, and chevron and triangle. Ellipsoidal and spherical dimples can be fabricated using LST or vibro-mechanical texturing [30, 36]. The other dimple shapes, which have vertical walls and a flat bottom profile, can be manufactured using lithography [28], RIE [26], or jet machining [27]. Figure 2 and Table 1 show the different dimple shapes, and the equations describing their geometry. The ellipsoidal dimple consists of a segment of an oblate ellipsoid of revolution, oriented symmetric with respect to the  $xz$  plane (flow direction). A special case of this ellipsoidal dimple occurs when the axes in the  $x$ - and  $y$ -directions have the same length, reducing the ellipsoidal dimple to a spherical dimple (Fig. 2a, b). The elliptical and circular dimples are cylindrical dimples with a flat bottom profile, vertical dimple walls and elliptical or circular cross-section, respectively (Fig. 2c, d). The chevron-shaped dimple is defined by two similar equilateral triangles of different sizes, and has a flat bottom profile with vertical dimple wall. The triangular dimple is a special case of the

chevron-shaped dimple with the inner edge length of the chevron equal to zero. The center point of the dimple coincides with that of the unit cell for all dimple shapes except for the chevron and triangle shaped dimples. For these two cases, the center of the unit cell coincides with the midpoint of the altitude line of the triangle or chevron shape. This allows achieving a higher texture density than locating the shape in the same way as the other dimple shapes. The triangular shape is only investigated for the orientation shown (Fig. 2e, f).

The aspect ratio  $\varepsilon$  and the texture density  $S_p$  uniquely describe the patterned texture (Table 1). For the ellipsoidal and elliptical dimples two aspect ratios,  $\varepsilon_1$  and  $\varepsilon_2$ , are introduced to completely define the dimple geometry. For these two shapes, the largest possible texture density depends on the ratio of the lengths of two axes of the dimple, i.e., the ratio of two aspect ratios  $\varepsilon_1/\varepsilon_2$ . The maximum texture density is found to be

$$S_{p,max} = \frac{\pi}{4} \cdot \min\left(\frac{\varepsilon_1}{\varepsilon_2}, \frac{\varepsilon_2}{\varepsilon_1}\right) \tag{4a}$$

with

$$\frac{4S_p}{\pi} \leq \frac{\varepsilon_1}{\varepsilon_2} \leq \frac{\pi}{4S_p}, \tag{4b}$$

for any given  $S_p$ , because only a limited range of  $\varepsilon_1/\varepsilon_2$  values (Eq. 4b) can satisfy the  $S_p$  requirement.

Spherical and circular dimples can achieve the largest texture density among all dimple shapes considered in this study. For a circle within a square cell, the area density is constrained to  $\pi/4$  when the circle touches all four edges of the cell. This value is also consistent with Eq. (4) when  $\varepsilon_1 = \varepsilon_2$ . Chevron-shaped dimples, need an extra parameter  $K$  to describe the ratio of the size of the inner equilateral triangle to the outer one ( $K < 1$ ). The maximum texture density that can be obtained depends on the value of  $K$ .

$$S_{p,max} = \frac{\sqrt{3}}{4} (1 - K^2) \tag{5a}$$

with

$$K \leq \sqrt{1 - \frac{4\sqrt{3}}{3} S_p}, \tag{5b}$$

for any given  $S_p$ . When  $K = 0$ , the chevron-shaped dimple is reduced to a triangular dimple with  $S_{p,max} = \sqrt{3}/4$ .

Equation (6) describes the non-dimensional local spacing  $H(X,Y)$  between the textured surface and the flat surface within one unit cell (origin is located as shown in Fig. 2), as a function of the aspect ratio  $\varepsilon$  and non-dimensional minimum spacing  $\delta$ , for the different dimple shapes outlined in Table 1.

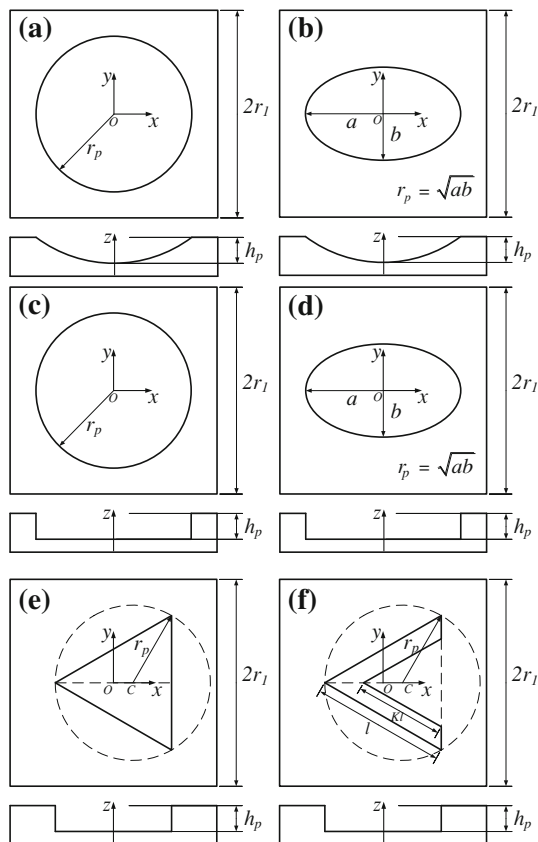


**Fig. 2** Different dimple shapes and geometries: **a** sphere, **b** ellipsoid, **c** circle, **d** ellipse, **e** triangle, **f** chevron

$$H(X, Y) = \begin{cases} 1, & \text{if } X^2 + Y^2 > 1 \\ 1 + \frac{1}{2\delta} \sqrt{\left(\varepsilon + \frac{1}{4\varepsilon}\right)^2 - (X^2 + Y^2)} - \frac{1}{2\delta} \left(\frac{1}{4\varepsilon} - \varepsilon\right), & \text{if } X^2 + Y^2 \leq 1 \end{cases} \quad (6a)$$

$$H(X, Y) = \begin{cases} 1, & \text{if } \frac{\varepsilon_1}{\varepsilon_2} X^2 + \frac{\varepsilon_2}{\varepsilon_1} Y^2 > 1 \\ 1 + \frac{1}{2\delta} \sqrt{\frac{\varepsilon_1}{\varepsilon_2} \left(\varepsilon_2 + \frac{1}{4\varepsilon_2}\right)^2 - \frac{\varepsilon_1}{\varepsilon_2} X^2 - \frac{\varepsilon_2}{\varepsilon_1} Y^2} - \frac{1}{2\delta} \sqrt{\frac{\varepsilon_1}{\varepsilon_2}} \left(\frac{1}{4\varepsilon_2} - \varepsilon_2\right), & \text{if } \frac{\varepsilon_1}{\varepsilon_2} X^2 + \frac{\varepsilon_2}{\varepsilon_1} Y^2 \leq 1 \end{cases} \quad (6b)$$

$$H(X, Y) = \begin{cases} 1, & \text{if } X^2 + Y^2 > 1 \\ 1 + \frac{\varepsilon}{\delta}, & \text{if } X^2 + Y^2 \leq 1 \end{cases} \quad (6c)$$

$$H(X, Y) = \begin{cases} 1, & \text{if } \frac{\varepsilon_1}{\varepsilon_2} X^2 + \frac{\varepsilon_2}{\varepsilon_1} Y^2 > 1 \\ 1 + \frac{\sqrt{\varepsilon_1 \varepsilon_2}}{\delta}, & \text{if } \frac{\varepsilon_1}{\varepsilon_2} X^2 + \frac{\varepsilon_2}{\varepsilon_1} Y^2 \leq 1 \end{cases} \quad (6d)$$

$$H(X, Y) = \begin{cases} 1, & \text{if } (X, Y) \notin \Omega \\ 1 + \frac{\varepsilon}{\delta}, & \text{if } (X, Y) \in \Omega \end{cases}$$

$$\Omega : -\frac{3}{4} \leq X \leq \frac{3}{4} \text{ and } -\frac{1}{\sqrt{3}}X - \frac{\sqrt{3}}{4} \leq Y \leq \frac{1}{\sqrt{3}}X + \frac{\sqrt{3}}{4} \quad (6e)$$

finite difference approach on a staggered grid [45] with an over-relaxation factor of 1.4. Because of symmetry with respect to the flow direction ( $x$ -direction) only half of the domain is solved. Convergence of the pressure solution is obtained to within 0.01 % change between two successive iterations at each node of the computational grid. A uniform Cartesian grid with 251 by 251 nodes per unit cell is selected based on a convergence and accuracy analysis, i.e., further refining the grid did not change the solution in excess of 2 %.

$$H(X, Y) = \begin{cases} 1, & \text{if } (X, Y) \notin \Omega \\ 1 + \frac{\varepsilon}{\delta}, & \text{if } (X, Y) \in \Omega \end{cases}$$

$$\Omega : -\frac{3}{4} \leq X \leq \frac{3}{4} \text{ and } \begin{cases} \frac{1}{\sqrt{3}}X + \frac{\sqrt{3}}{2} \left(K - \frac{1}{2}\right) \leq Y \leq \frac{1}{\sqrt{3}}X + \frac{\sqrt{3}}{4}, & \text{if } Y \geq 0 \\ -\frac{1}{\sqrt{3}}X - \frac{\sqrt{3}}{4} \leq Y \leq -\frac{1}{\sqrt{3}}X + \frac{\sqrt{3}}{2} \left(\frac{1}{2} - K\right), & \text{if } Y \leq 0 \end{cases} \quad (6f)$$

### 3 Results and Discussion

#### 3.1 Simulation Method

The operating conditions of the textured parallel slider bearing are fixed as  $\delta = 2.0 \times 10^{-3}$  and  $\lambda = 2.0 \times 10^{-5}$  throughout the numerical simulations performed in this paper. These values are typical for applications as, for instance, magnetic tape drives [23]. Only in Sect. 3.4, the optimal texture density and aspect ratio are investigated as a function of the operating parameters. For each of the six dimple shapes, the aspect ratio  $\varepsilon$  ( $\varepsilon_1, \varepsilon_2$  for elliptical and ellipsoidal shapes), texture density  $S_p$ , and  $K$  (for chevron-shaped dimples only), are considered over their entire range of possible values. Equations (2) and (3) are solved for a column of ten dimple cells using a central discretization

#### 3.2 Optimization of Different Dimple Shapes

##### 3.2.1 Spherical, Circular, and Triangular Dimples

Figures 3, 4, and 5 show the non-dimensional net average bearing pressure as a function of the texture density and the dimple aspect ratio, for spherical, circular, and triangular dimple shapes, respectively. The  $x$ -axis is limited to the  $S_{p,max}$  value listed in Table 1. It is observed that for the three dimple shapes the average bearing pressure is the highest for  $0.1 < S_p < 0.3$  and  $\varepsilon < 0.01$ . The optimal texture density decreases with increasing dimple aspect ratio, indicating that with a deeper dimple profile, fewer dimples per unit area are needed to produce the maximum pressure. The results for spherical dimples agree well with the results obtained by Raeymaekers et al. [23] who found an

**Table 1** Analytical description of the different dimple shape geometries

Category	Shape	Non-dimensional parameters	Maximum texture density	$H(X,Y)$
Ellipsoid	Sphere	$\varepsilon = \frac{h_p}{2r_p}$ $S_p = \frac{\pi r_p^2}{4r_1^2}$	$S_{p,max} = \frac{\pi}{4}$	Eq. (6a)
	Ellipsoid	$\varepsilon_1 = \frac{h_p}{2a}, \varepsilon_2 = \frac{h_p}{2b}$ $S_p = \frac{\pi r_p^2}{4r_1^2} = \frac{\pi ab}{4r_1^2}$	$S_{p,max} = \frac{\pi}{4} \cdot \min\left(\frac{\varepsilon_1}{\varepsilon_2}, \frac{\varepsilon_2}{\varepsilon_1}\right)$	Eq. (6b)
Ellipse	Circle	Identical as sphere		Eq. (6c)
	Ellipse	Identical as ellipsoid		Eq. (6d)
Chevron	Triangle	$\varepsilon = \frac{h_p}{2r_p}$ $S_p = \frac{3\sqrt{3}r_p^2}{16r_1^2}$	$S_{p,max} = \frac{\sqrt{3}}{4}$	Eq. (6e)
	Chevron	$\varepsilon = \frac{h_p}{2r_p}$ $S_p = \frac{3\sqrt{3}(1-K^2)r_p^2}{16r_1^2}$ $K$	$S_{p,max} = \frac{\sqrt{3}}{4}(1-K^2)$	Eq. (6f)

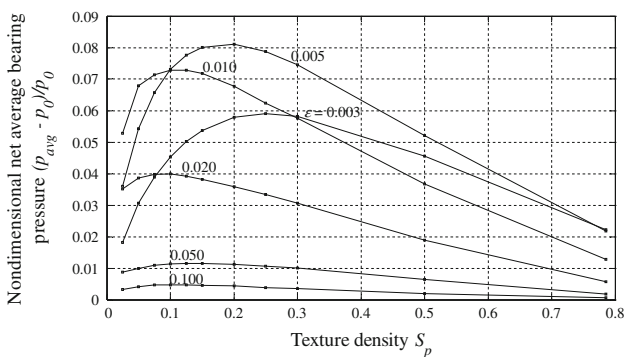


**Fig. 3** Non-dimensional net average bearing pressure for spherical dimples as a function of  $S_p$  for different  $\varepsilon$  values

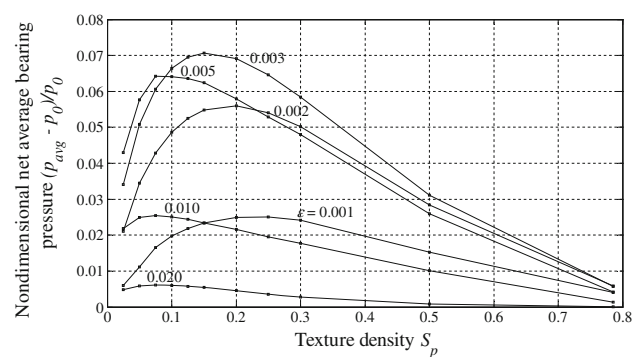


**Fig. 4** Non-dimensional net average bearing pressure for circular dimples as a function  $S_p$  for different  $\varepsilon$  values

optimum for spherical dimples with  $0.1 < S_p < 0.3$  and  $0.003 < \varepsilon < 0.05$ . The maximum non-dimensional net average bearing pressure for each of these dimple shapes are found as:  $S_p = 0.150$  and  $\varepsilon = 0.007$  for the spherical dimple shape,  $S_p = 0.150$  and  $\varepsilon = 0.0035$  for the circular

shape, and  $S_p = 0.100$  and  $\varepsilon = 0.0035$  for the triangular shape. This results in non-dimensional net bearing pressure values of 0.0852, 0.0727, and 0.0514, respectively.

Figure 6 shows the non-dimensional net pressure along the centerline of a column of ten dimples for the optimized

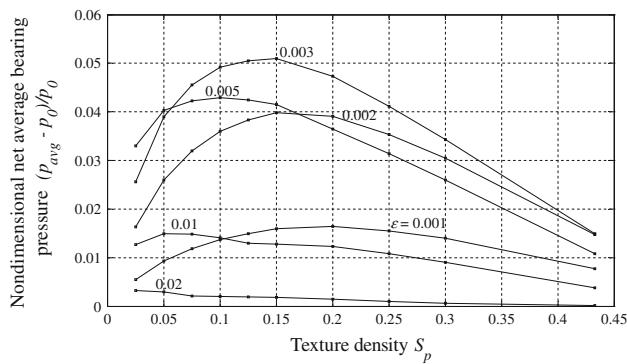


**Fig. 5** Non-dimensional net average bearing pressure for triangular dimples as a function of  $S_p$  for different  $\varepsilon$  values

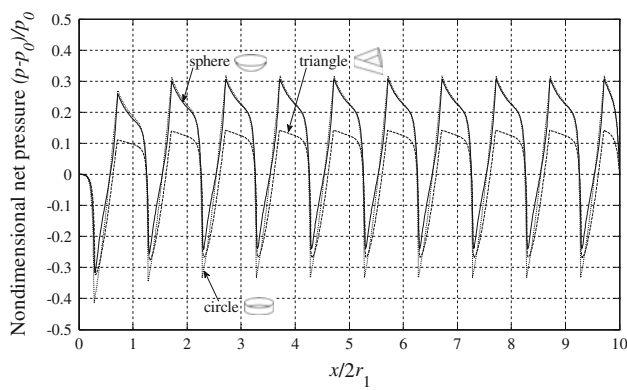


**Fig. 6** Non-dimensional net pressure along the center line of a column of ten dimples: optimal spherical, circular, and triangular dimple geometries

geometry of these three different dimple shapes. It is observed that for the spherical dimple, the pressure rises and decreases to approximately 1.3 and 0.78 times the atmospheric pressure, respectively. Corresponding maximum and minimum pressure values are 1.3 and 0.68 times the atmospheric pressure for the circular dimple, and 1.14 and 0.74 for the triangular dimple. It is also noticed that for each of the three dimple shapes, the pressure distribution becomes periodic after two dimples.

### 3.2.2 Ellipsoidal, Elliptical, and Chevron-Shaped Dimples

Figures 7 and 8 display the non-dimensional net average pressure contour lines for ellipsoidal and elliptical dimples for  $S_p = 0.050, 0.175, 0.350,$  and  $0.500,$  respectively. The domain of feasible combinations of  $\varepsilon_1$  and  $\varepsilon_2$  to obtain the desired  $S_p$  is bound according to Eq. (4b). For each  $S_p$  value, an optimal  $\varepsilon_1/\varepsilon_2$  exists that maximizes the non-dimensional net average bearing pressure, which is indicated by a “+” marker in Figs. 7 and 8.

From Figs. 7 and 8, we observe that the optimal ratio of  $\varepsilon_1/\varepsilon_2$  changes from  $\varepsilon_1/\varepsilon_2 < 1$  to  $\varepsilon_1/\varepsilon_2 > 1$  with increasing

$S_p$ . As a result, the optimal ellipsoid/ellipse dimple shape changes from orienting the long axis in the flow direction ( $x$ -direction) to orienting the long axis orthogonal to the flow direction ( $y$ -direction). This result can be explained as follows.

Figure 9 presents the dimple geometry of the optimized ellipsoidal dimples for different  $S_p$  values indicated in the figure. It appears that a finite size of the dimple is necessary in the streamwise direction for the texture to be functional, i.e., generating hydrodynamic pressure. Hence, for a small texture density (e.g.,  $S_p = 0.05$ ), the optimal dimple geometry commands the longitudinal axis of the ellipsoid to be placed in the flow direction. However, when increasing  $S_p$ , the optimal geometry is found to expand in the spanwise direction of the unit cell, thus placing the longitudinal axis of the ellipsoid orthogonal to the flow direction. For a certain  $S_p$ , the optimal geometry stretches out to the lateral edges of the unit cell. When further increasing  $S_p$ , the dimple can only stretch in the flow direction, thus locating the optimum right on the boundary of the domain of feasible  $\varepsilon_1/\varepsilon_2$  combinations (Figs. 7, 8).

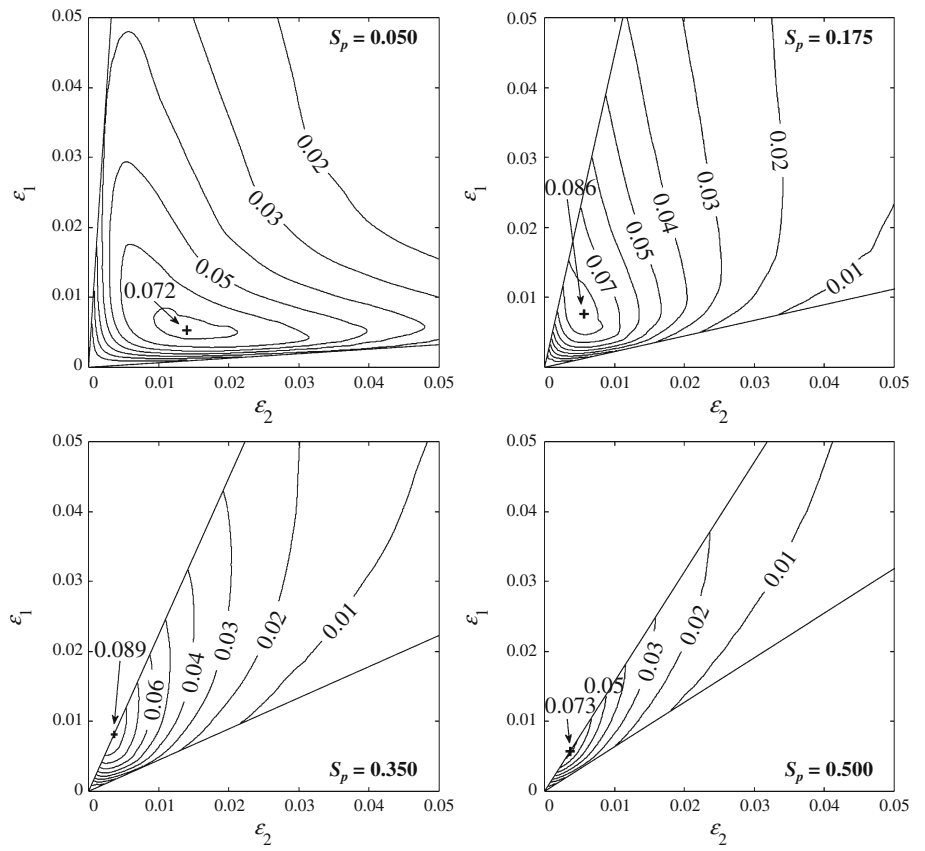
For chevron-shaped dimples, the ratio of the inner triangle size to the outer triangle size  $K$  is needed in addition to  $\varepsilon$  and  $S_p$  (as indicated in Fig. 2f). Figure 10 shows contour plots of the non-dimensional net average bearing pressure as a function of  $\varepsilon$  and  $K$  for  $S_p = 0.050, 0.010, 0.175,$  and  $0.350,$  respectively, with the optimum indicated by a “+” marker in each figure. The non-dimensional net average pressure changes quickly when  $\varepsilon < 0.01$ , but is less sensitive to  $K$ , i.e., using a triangular-shaped versus a chevron-shaped dimple affects the bearing pressure less than changing the aspect ratio of either shape. In addition, the optimal combination of  $\varepsilon$ , and  $K$  is almost independent of  $S_p$ . The optimal chevron-shaped dimple is found to be  $S_p = 0.100, \varepsilon = 0.0035, K = 0.300,$  generating a maximum non-dimensional net average bearing pressure of 0.0542.

Figure 11 shows the non-dimensional pressure along the centerline of a column of ten dimples for the optimized geometry of these three different dimple shapes. It is observed that for the ellipsoidal dimple, the pressure rises and decreases to approximately 1.23 and 0.82 times the atmospheric pressure, respectively. Corresponding maximum and minimum pressure values are 1.25 and 0.72 times the atmospheric pressure for the elliptical dimple, and 1.12 and 0.74 for the chevron-shaped dimple.

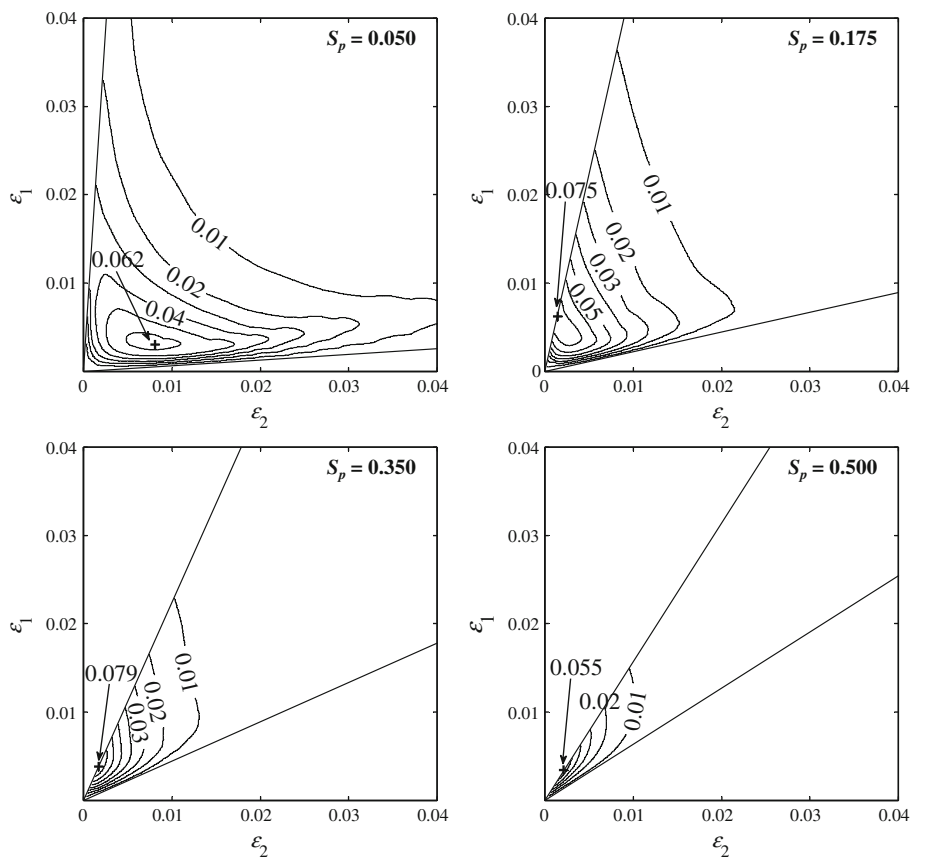
### 3.3 Comparison of the Performance of Different Dimple Shapes

The performance of the six different texture shapes is compared relative to each other. For each shape, the

**Fig. 7** Non-dimensional net average bearing pressure contour plots for ellipsoidal dimple shapes as a function of aspect ratio combinations for  $S_p = 0.050, 0.175, 0.350,$  and  $0.500$  (“+” marker indicates the optimal combination)



**Fig. 8** Non-dimensional net average bearing pressure contour plots for elliptical dimple shapes as a function of aspect ratio combinations for  $S_p = 0.050, 0.175, 0.350,$  and  $0.500$  (“+” marker indicates the optimal combination)



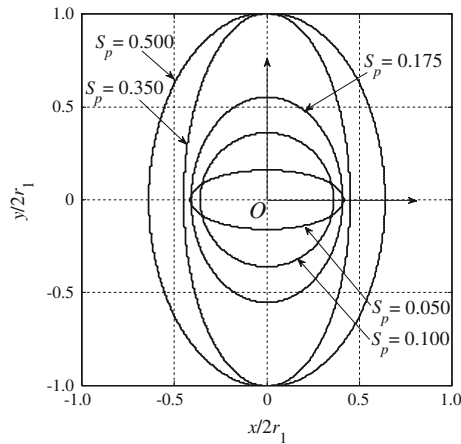


**Fig. 9** Optimal dimple geometry of ellipsoidal dimples for different  $S_p$  values (flow along  $x$ -direction)

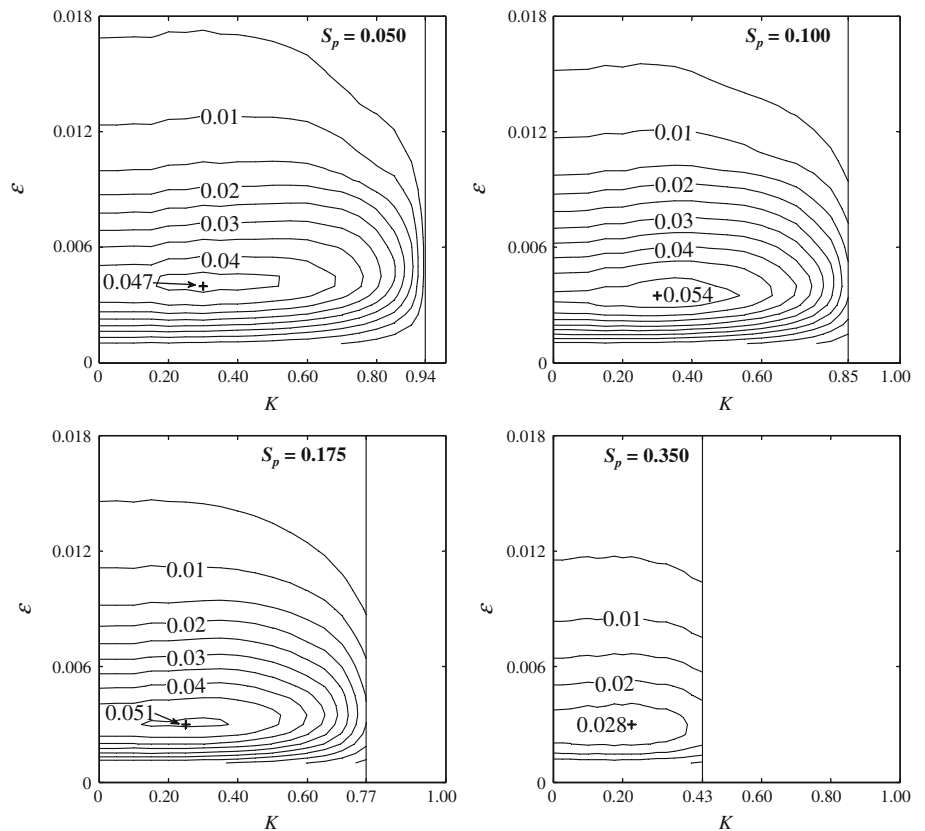
optimized texture geometry that yields maximum average bearing pressure is summarized in Table 2.

Significant differences exist in the optimized net average bearing pressure (load-carrying capacity), depending on the texture shape used. For the same contour shape, the dimple shapes with a curved bottom profile outperform the shapes with a flat bottom profile in terms of net average bearing pressure, which is in line with the results by Pinkus and Sternlicht [44] who determined the analytical solution of an infinitely long gas bearing and found that a composite slider

combining an inclined slider and a flat against a smooth plane performs better than a step bearing. Moreover, the average bearing pressure is 4.5 % larger for ellipsoidal dimples than for spherical dimples, each with optimized geometry. A detailed examination reveals that the optimum of the former has almost the same length in the flow direction as the latter, but the former expands further orthogonal to the flow direction, which results in a larger dimple volume, thus compressing more lubricant. This small gain in load-carrying capacity likely does not justify the use of ellipsoidal dimples, which are more difficult to manufacture than spherical dimples. The triangular and chevron-shaped dimples are the least effective in terms of generating hydrodynamic pressure.

When comparing the optimal texture parameters it is found that the contour of the dimple shape seems to define the optimal texture density, while the bottom profile of the dimple dictates the optimal aspect ratio. From Table 2, it is observed that the optimal  $S_p$  is identical for the sphere- and circle-shaped dimples, ellipse- and ellipsoid-shaped dimples, and triangle- and chevron-shaped dimples, respectively. In fact, the optimal ellipsoidal and elliptical dimples have almost identical  $\varepsilon_1/\varepsilon_2$  ratio, indicating that both dimples are described by the same contour. For a particular dimple shape and the corresponding optimal texture density, an optimum dimple volume seems to exist, which defines the optimal aspect ratio based on the bottom profile of the dimple. Table 3 shows the non-dimensional dimple

**Fig. 10** Non-dimensional net average bearing pressure contour plots for chevron-shaped dimples as a function of  $\varepsilon$  and  $K$  for different  $S_p$  values,  $K$  spans the full range within the constraint to obtain a specific  $S_p$  (“+” marker indicates the optimal combination)



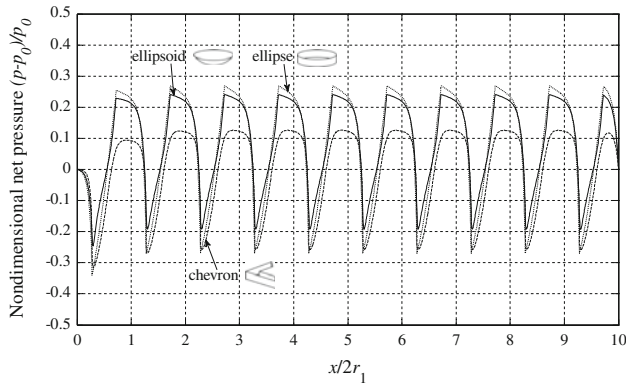


**Fig. 11** Non-dimensional net pressure along the center line of a column of ten dimples: optimal ellipsoidal, elliptical and chevron-shaped dimple geometries

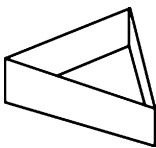
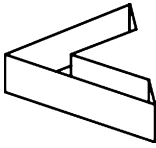
volume calculated from the optimal parameters in Table 2, non-dimensionalized by the volume of a cube unit cell,  $(2r_1)^3$ . It can be seen that the optimized dimple shapes with

the same contour shape (e.g., circle and sphere, ellipse and ellipsoid) result in almost identical non-dimensional volume, regardless of the bottom profile of the dimple (flat or curved). The optimal triangle- and chevron-shaped dimple geometries result in similar dimple volumes since the optimal  $K$  is small and the change of the  $K$  value has only a small effect on the results, as is shown in Fig. 10.

### 3.4 Effect of Different Operating Conditions

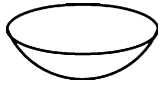
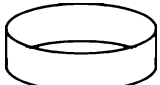
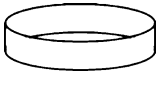
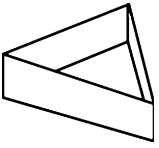
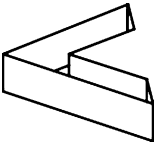
Spherical dimples are used as an example to evaluate the effect of operating conditions ( $\lambda$ ,  $\delta$ ) on the optimal texture aspect ratio  $\varepsilon$ . Figures 12 and 13 show the non-dimensional net average bearing pressure as a function of  $\varepsilon$  for different values of  $\lambda$  and  $\delta$ . It is observed that with increasing  $\lambda$  (increasing sliding speed or lubricant viscosity) the load-carrying capacity increases. The optimal  $\varepsilon$  increases slightly with increasing  $\lambda$ . For instance for  $\lambda = 1.0 \times 10^{-5}$  the optimum  $\varepsilon = 0.005$ , while for  $\lambda = 3.5 \times 10^{-5}$  the

**Table 2** Optimal texture parameters for different texture shapes and corresponding maximum net average pressure

Dimple shape	Optimized texture geometry and texture density	Non-dimensional net average pressure	Relative net average pressure
Sphere	$S_p = 0.150, \varepsilon = 0.0070$	0.0852	0
			
Circle	$S_p = 0.150, \varepsilon = 0.0035$	0.0727	-14.7 %
			
Ellipsoid	$S_p = 0.350, \varepsilon_1 = 0.0081, \varepsilon_2 = 0.0036$	0.0890	+4.5 %
			
Ellipse	$S_p = 0.350, \varepsilon_1 = 0.0038, \varepsilon_2 = 0.0017$	0.0786	-7.8 %
			
Triangle	$S_p = 0.100, \varepsilon = 0.0035$	0.0514	-39.7 %
			
Chevron	$S_p = 0.100, \varepsilon = 0.0035, K = 0.300$	0.0542	-36.4 %
			

The relative net average pressure is calculated as a percent difference relative to the non-dimensional net average pressure obtained for spherical dimples

**Table 3** Non-dimensional dimple volume for optimal dimple shapes

Shape	Sphere	Circle	Ellipsoid	Ellipse	Triangle	Chevron
						
Non-dimensional dimple volume	$2.29 \times 10^{-4}$	$2.29 \times 10^{-4}$	$6.31 \times 10^{-4}$	$5.94 \times 10^{-4}$	$1.94 \times 10^{-4}$	$2.04 \times 10^{-4}$

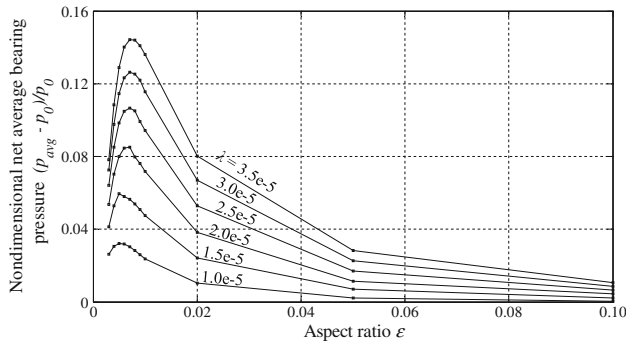


**Fig. 12** Non-dimensional net average bearing pressure as a function of dimple aspect ratio for spherical dimples ( $S_p = 0.15$ ),  $\delta = 0.002$ , for different  $\lambda$

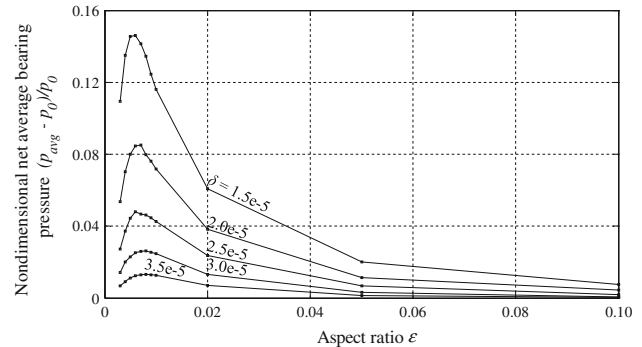


**Fig. 13** Non-dimensional net average bearing pressure as a function of dimple aspect ratio for spherical dimples ( $S_p = 0.15$ ),  $\lambda = 2.0e-5$ , for different  $\delta$

optimum  $\epsilon = 0.0075$ . This trend corresponds to the results found by Ma and Zhu [46]. On the other hand, reducing the spacing  $\delta$  causes the load-carrying capacity to increase, which is expected because the bearing stiffens. The optimal  $\epsilon$  remains almost constant as a function of  $\delta$ , depicted in Fig. 13. Both results indicate that the operating conditions only have a limited effect on the optimal geometry parameters of a given dimple shape.

### 3.5 Practical Considerations

It should be noted that the results obtained for all dimple shapes suffer from inaccuracies as a result of the finite difference grid, caused by a discontinuous film thickness gradient at the edges of the dimple. The discontinuous transition between the dimple wall and bottom is approximated by an inclined dimple wall after discretization, as opposed to a vertical wall [47]. Because adjacent grid points are separated by a finite distance, a vertical dimple wall cannot be achieved. The dimple wall deviates from a vertical wall by an angle  $\theta$

$$\theta \cong \tan(\theta) = \frac{\Delta x}{h_p} = \frac{1}{n\epsilon} \frac{r_1}{r_p} \cong \frac{1}{n\epsilon} \sqrt{\frac{1}{S_p}}, \quad (7)$$

where  $n$  denotes the number of grid intervals along the length of a unit dimple cell, and  $\Delta x$  is the grid spacing. The

simulations in this paper use  $n = 250$ , and, e.g.,  $\epsilon = 0.001$  and  $S_p = 0.025$ , which results in  $\theta = 25^\circ$ . All dimples considered are very shallow, typically with  $\epsilon$  on the order of  $10^{-2}$  or  $10^{-3}$ , and the inaccuracy is insignificant. In fact, it has been shown that local inaccuracies in the pressure calculation have little effect on simulation of the load-carrying capacity in gas bearing applications [48].

While an unconstrained optimization of the geometry of each dimple shape is performed in terms of maximum load-carrying capacity per unit area, it should be pointed out that the categories of dimple shapes are not comprehensive. A true general framework would require the dimple geometry to be optimized in two or three dimensions by for instance using a genetic algorithm, rather than only comparing several commonly used texture shapes. In addition, experimental validation is necessary to examine the load-carrying capacity predicted by this study.

The texture parameters can also be optimized in an alternative fashion, friendlier to bearing designers. In engineering practice, the operating conditions typically specify the load-carrying capacity rather than the bearing spacing. By defining the load-carrying capacity per unit area as the net average pressure for the dimple column problem, the steady-state non-dimensional bearing spacing  $\delta$  can be found by solving Eqs. (2) and (3), by iteratively changing  $\delta$ . Figure 14 shows the non-dimensional spacing  $\delta$  as a function of  $S_p$  for different  $\epsilon$

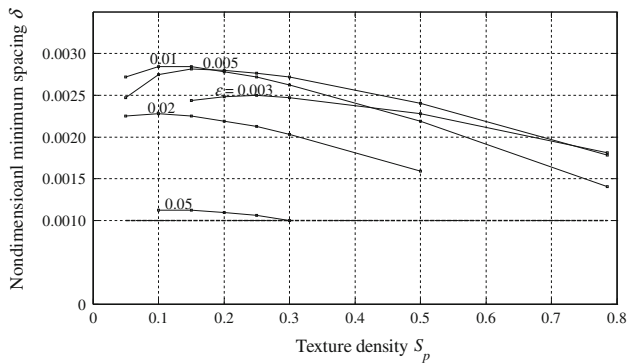


**Fig. 14** non-dimensional spacing  $\delta$  for spherical dimples as a function of  $S_p$  for different  $\varepsilon$  values (non-dimensional net average bearing pressure 0.03)

values. Spherical dimples are used, and the bearing is designed with a non-dimensional net average bearing pressure of 0.03. The results agree well with those obtained for spherical dimples by specifying the spacing and solving for the load-carrying capacity (Fig. 3), and the optimum is found to be  $\varepsilon = 0.007$  and  $S_p$  between 0.15 and 0.2. The values for  $\delta$  cannot be obtained for all the combinations of  $\varepsilon$  and  $S_p$  because for some of the extreme geometries a non-dimensional spacing  $\delta$  larger than 0.001 (indicated by the dashed line in Fig. 14) cannot be obtained, which would likely violate one of the model's assumptions that hydrodynamic lubrication is maintained at all time. This approach can be used to determine the spacing between the sliding surfaces that a certain texture pattern can provide under a prescribed load condition. Alternatively, it can be used to define the requirement for surface smoothness to achieve hydrodynamic lubrication with a specific textured parallel bearing.

Finally, while in this paper, the optimization is carried out in terms of maximum load-carrying capacity, the effect of dimple shape on the friction coefficient and the stiffness of the bearing can be evaluated as well using the same framework.

#### 4 Conclusion

In this paper, six different dimple shapes were optimized in terms of load-carrying capacity for use in the general case of air lubricated textured parallel bearings. The performance of each dimple shape, with optimized geometry, was then compared relative to each other. No constraints were used when optimizing the geometry of each of the different dimple shapes. We conclude that

- (1) For each of the dimple shapes considered, the optimal geometry was found to be in the range of  $0.001 < \varepsilon < 0.010$  and  $0.10 < S_p < 0.35$ .
- (2) The contour of the dimple shape seems to define the optimal texture density, while the optimal aspect ratio

is dictated by the optimal volume and the bottom profile of the dimple.

- (3) The ellipsoidal dimple was found to provide the maximum load-carrying capacity of all shapes considered in this study. The optimum identified in this study is  $S_p = 0.35$ ,  $\varepsilon_1 = 0.0081$ ,  $\varepsilon_2 = 0.0036$ , producing a net average pressure of 0.0890, which is only 4.5 % higher than the optimized spherical dimples. Considering that spherical dimples are easier to manufacture than ellipsoidal dimples, it may be more cost effective to use the former, despite the superior performance of the ellipsoidal dimples. It was also found that the optimal geometry seems to almost be independent of the operating conditions.

**Acknowledgments** The authors wish to thank Professor Izhak Etsion from the Technion in Haifa, Israel, for fruitful discussions and insightful comments.

#### References

1. Etsion, I.: State of the art in laser surface texturing. *J. Tribol. Trans. ASME* **127**, 248–253 (2005)
2. Etsion, I., Kligerman, Y., Halperin, G.: Analytical and experimental investigation of laser-textured mechanical seal faces. *Tribol. Trans.* **42**, 511–516 (1999)
3. McNickle, A.D., Etsion, I.: Near-contact laser surface textured dry gas seals. *J. Tribol. Trans. ASME* **126**, 788–794 (2004)
4. Varenberg, M., Halperin, G., Etsion, I.: Different aspects of the role of wear debris in fretting wear. *Wear* **252**, 902–910 (2002)
5. Volchok, A., Halperin, G., Etsion, I.: The effect of surface regular micro-topography on fretting fatigue life. *Wear* **253**, 509–515 (2002)
6. Kovalchenko, A., Ajayi, O., Erdemir, A., Fenske, G., Etsion, I.: The effect of laser surface texturing on transitions in lubrication regimes during unidirectional sliding contact. *Tribol. Int.* **38**, 219–225 (2005)
7. Kovalchenko, A., Ajayi, O., Fenske, G., Etsion, I.: The effect of laser texturing of steel surfaces and speed-load parameters on the transition of lubrication regime from boundary to hydrodynamic. *Tribol. Trans.* **47**, 299–307 (2004)
8. Wang, X., Adachi, K., Otsuka, K., Kato, K.: Optimization of the surface texture for silicon carbide sliding in water. *Appl. Surf. Sci.* **253**, 1282–1286 (2006)
9. Galda, L., Pawlus, P., Sep, J.: Dimple shape and distribution effect on characteristics of stribeck curve. *Tribol. Int.* **42**, 1505–1512 (2009)
10. Raeymaekers, B., Etsion, I., Talke, F.E.: Enhancing tribological performance of the magnetic tape/guide interface by laser surface texturing. *Tribol. Lett.* **27**, 89–95 (2007)
11. Lu, X., Khonsari, M.M.: An experimental investigation of dimple effect on the stribeck curve of journal bearings. *Tribol. Lett.* **27**, 169–176 (2007)
12. Tala-Ighil, N., Maspeyrot, P., Fillon, M., Bounif, A.: Effects of surface texture on journal-bearing characteristics under steady-state operating conditions. *Proc. Inst. Mech. Eng. J* **221**, 623–633 (2007)

13. Cupillard, S., Glavatskih, S., Cervantes, M.J.: Computational fluid dynamics analysis of a journal bearing with surface texturing. *Proc. Inst. Mech. Eng. J* **222**, 97–107 (2008)
14. Wang, X., Kato, K., Adachi, K., Aizawa, K.: Loads carrying capacity map for the surface texture design of SiC thrust bearing sliding in water. *Tribol. Int.* **36**, 189–197 (2003)
15. Brizmer, V., Kligerman, Y., Etsion, I.: A laser surface textured parallel thrust bearing. *Tribol. Trans.* **46**, 397–403 (2003)
16. Etsion, I., Halperin, G., Brizmer, V., Kligerman, Y.: Experimental investigation of laser surface textured parallel thrust bearings. *Tribol. Lett.* **17**, 295–300 (2004)
17. Rahmani, R., Shirvani, A., Shirvani, H.: Optimization of partially textured parallel thrust bearings with square-shaped micro-dimples. *Tribol. Trans.* **50**, 401–406 (2007)
18. Ronen, A., Etsion, I., Kligerman, Y.: Friction-reducing surface-texturing in reciprocating automotive components. *Tribol. Trans.* **44**, 359–366 (2001)
19. Etsion, I., Burstein, L.: A model for mechanical seals with regular microsurface structure. *Tribol. Trans.* **39**, 677–683 (1996)
20. Hoppermann, A., Kordt, M.: Tribological optimisation using laser-structured contact surfaces. *O+P Oelhydraulik und Pneumatik*, vol. 46 (2002). Vereinigte Fachverlage, Mainz. ISSN 0341-2660
21. Yu, X.Q., He, S., Cai, R.L.: Frictional characteristics of mechanical seals with a laser-textured seal face. *J. Mater. Process. Technol.* **129**, 463–466 (2002)
22. Feldman, Y., Kligerman, Y., Etsion, I.: A hydrostatic laser surface textured gas seal. *Tribol. Lett.* **22**, 21–28 (2006)
23. Raeymaekers, B., Etsion, I., Talke, F.E.: A model for magnetic tape/guide friction reduction by laser surface texturing. *Tribol. Lett.* **28**, 9–17 (2007)
24. Schneider, Y.G.: Formation of surfaces with uniform micropatterns on precision machine and instruments parts. *Precis. Eng.* **6**, 219–225 (1984)
25. Saka, N., Tian, H., Suh, N.P.: Boundary lubrication of undulated metal surfaces at elevated temperatures. *Tribol. Trans.* **32**, 385–389 (1989)
26. Wang, X., Kato, K.: Improving the anti-seizure ability of SiC seal in water with RIE texturing. *Tribol. Lett.* **14**, 275–280 (2003)
27. Wakuda, M., Yamauchi, Y., Kanzaki, S., Yasuda, Y.: Effect of surface texturing on friction reduction between ceramic and steel materials under lubricated sliding contact. *Wear* **254**, 356–363 (2003)
28. Pettersson, U., Jacobson, S.: Influence of surface texture on boundary lubricated sliding contacts. *Tribol. Int.* **36**, 857–864 (2003)
29. Stephens, L.S., Siripuram, R., Hyden, M., McCartt, B.: Deterministic micro asperities on bearings and seals using a modified LIGA process. *J. Eng. Gas Turb. Power* **126**, 147–154 (2004)
30. Greco, A., Raphaelson, S., Ehmann, K., Wang, Q.J.: Surface texturing of tribological interfaces using the vibromechanical texturing method. *J. Manuf. Sci. E* **131**, 1–8 (2009)
31. Scott, D.A., Brandt, M., Dorien-Brown, B., Valentine, B., De, P.: Laser modification of metal surfaces. *Opt. Lasers Eng.* **18**, 1–13 (1993)
32. Geiger, M., Roth, S., Becker, W.: Influence of laser-produced microstructures on the tribological behavior of ceramics. *Surf. Coat. Tech.* **100–101**, 17–22 (1998)
33. Dumitru, G., Romano, V., Weber, H.P., Haefke, H., Gerbig, Y., Pfluger, E.: Laser microstructuring of steel surfaces for tribological applications. *Appl. Phys. A* **70**, 485–487 (2000)
34. Duffet, G., Sallamand, P., Vannes, A.B.: Improvement in friction by cw Nd:YAG laser surface treatment on cast iron cylindrical bore. *Appl. Surf. Sci.* **205**, 289–296 (2003)
35. Erdemir, A.: Review of engineered tribological interfaces for improved boundary lubrication. *Tribol. Int.* **38**, 249–256 (2005)
36. Vilhena, L.M., Sedlacek, M., Podgornik, B., Vizintin, J., Babnik, A., Mozina, J.: Surface texturing by pulsed Nd:YAG laser. *Tribol. Int.* **42**, 1496–1504 (2009)
37. Pascovici, M.D., Cicone, T., Fillon, M., Dobrica, M.B.: Analytical investigation of a partially textured parallel slider. *Proc. Inst. Mech. Eng. J* **223**, 151–158 (2009)
38. Nakano, M., Korenaga, A., Korenaga, A., Miyake, K., Murakami, T., Ando, Y., Usami, H., Sasaki, S.: Applying micro-texture to cast iron surfaces to reduce the friction coefficient under lubricated conditions. *Tribol. Lett.* **28**, 131–137 (2007)
39. Qiu, Y., Khonsari, M.M.: Experimental investigation of tribological performance of laser textured stainless steel rings. *Tribol. Int.* **44**, 635–644 (2011)
40. Kligerman, Y., Etsion, I.: Analysis of the hydrodynamic effects in a surface textured circumferential gas seal. *Tribol. Trans.* **44**, 472–478 (2001)
41. Siripuram, R.B., Stephens, L.S.: Effect of deterministic asperity geometry on hydrodynamic lubrication. *J. Tribol. Trans. ASME* **126**, 527–534 (2004)
42. Yu, H., Wang, X., Zhou, F.: Geometric shape effects of surface texture on the generation of hydrodynamic pressure between conformal contacting surfaces. *Tribol. Lett.* **37**, 123–130 (2010)
43. Raeymaekers, B., Etsion, I., Talke, F.E.: The influence of operating and design parameters on the magnetic tape/guide friction coefficient. *Tribol. Lett.* **25**, 161–171 (2006)
44. Pinkus, O., Sternlicht, B.: *Theory of hydrodynamic lubrication*. McGraw-Hill, New York (1961)
45. Hirsch, C.: *Numerical computation of internal and external flows*, vol. 1. Wiley, New York (1988)
46. Ma, C., Zhu, H.: An optimum design model for textured surface with elliptical-shape dimples under hydrodynamic lubrication. *Tribol. Int.* **44**, 987–995 (2011)
47. Dobrica, M.B., Fillon, M., Pascovici, M.D., Cicone, T.: Optimizing surface texture for hydrodynamic lubricated contacts using a mass-conserving numerical approach. *Proc. Inst. Mech. Eng. J* **224**, 737–750 (2010)
48. Feldman, Y., Etsion, I., Haber, S.: The validity of the Reynolds equation in modeling hydrostatic effects in gas lubricated textured parallel surfaces. *J. Tribol. Trans. ASME* **128**, 345–350 (2006)